

# Experimental Investigation of Concentrated Solar-driven Methane Dry Reforming over Ni/CeO<sub>2</sub> Porous Catalyst<sup>#</sup>

Shuzhan Ye<sup>1,2</sup>, Xiangyu Yan<sup>1</sup>, Haoyu Li<sup>1,2</sup>, Shiyang Yang<sup>1,2</sup>, Fan Jiao<sup>1,2</sup>, Qibin Liu<sup>1,2\*</sup>

1 Institute of Engineering Thermophysics, Chinese Academy of Sciences, Beijing 100190, PR China

2 University of Chinese Academy of Sciences, Beijing 100049, PR China

(Corresponding Author: qibinliu@iet.cn)

## ABSTRACT

Solar-driven methane dry reforming represents a promising approach for converting greenhouse gases into syngas using renewable energy, offering both environmental and energy benefits. However, conventional methane dry reforming systems are typically plagued by low solar-to-fuel conversion efficiency and limited syngas yield, primarily due to inefficient heat utilization and poor reactor scalability. In this study, a kilowatt-scale solar-driven methane dry reforming systems incorporating a cavity-type solar reactor and a self-synthesized porous Ni/CeO<sub>2</sub> catalysts was developed. The system was evaluated under varying feeding rates to identify its thermochemical performance. The results demonstrated that the new system achieves a maximum solar-to-fuel conversion efficiency of 33.26%, with CH<sub>4</sub> and CO<sub>2</sub> conversions of 69.36% and 66.50%, respectively, the product generation rate is the L/min level, and can operate continuously for over 8 hours. The work highlights the potential of porous Ni/CeO<sub>2</sub> catalysts in high-flux solar methane dry reforming systems. It presents a scalable and efficient method for solar-natural gas hybrid fuel production, offering valuable insights for industrial solar thermochemical applications.

**Keywords:** Solar fuel, methane dry reforming, solar-to-fuel efficiency, Ni/CeO<sub>2</sub>, thermochemical energy storage

## NONMENCLATURE

Abbreviations	
MDR	Methane dry reforming
RWGS	Reverse water-gas shift
Symbols	
$F$	Flow rate of gas, mol/s
$P$	Power of light irradiation, kW
$X$	Conversion rate of CH <sub>4</sub> or CO <sub>2</sub> , %
$\eta_{STF}$	Solar-to-fuel conversion efficiency, %

$\Delta H$	Standard heat of combustion, kJ/mol
------------	-------------------------------------

## 1. INTRODUCTION

The use of fossil fuels results in the emission of large amounts of CO<sub>2</sub> [1], which contributes to global warming and various environmental challenges, such as water pollution. Reducing the use of fossil fuels and seeking for alternative clean energy sources is a key trend in the global energy landscape [2]. Solar fuel production allows intermittent and unstable solar energy to be stored as stable chemical energy, facilitating long-term storage and transportation of solar energy [3]. The solar thermochemical approach, in which solar energy is concentrated and converted into thermal energy to drive thermochemical reactions, is considered to be one of the most effective methods for solar fuel production [4]. Through chemical reactions, low-grade solar thermal energy is converted into high-grade chemical energy, achieving efficient utilization of solar energy [5]. CH<sub>4</sub> and CO<sub>2</sub>, as two major greenhouse gases, are the primary contributors to global warming [6]. Methane dry reforming (MDR) can convert methane and carbon dioxide into industrially valuable syngas [7]. The integration of solar thermal energy with the MDR process through a thermochemical approach offers benefits such as replacing fossil fuels and mitigating greenhouse gas emissions.

In the solar-driven MDR process, porous materials, with their low relative density, large specific surface area, and complex structure, play a significant role in enhancing heat transfer and optimizing reaction conditions [8], thus improving energy conversion and storage efficiency [9] and achieving excellent photothermal performance [10]. Shi et al. [11] proposed a solar-driven MDR reactor with a biomimetic venous-porous structure, achieving a 5.9% increase in CH<sub>4</sub> conversion. Zhang et al. [12] improved solar-to-fuel efficiency by up to 2.43% through optimized porous

<sup>#</sup> This is a paper for the 11th Applied Energy Symposium: Low Carbon Cities & Urban Energy Systems (CUE2025), July 18-22, 2025, Kitakyushu, Japan.

ceramic arrangement in an MDR reactor. Zhang et al. [13] designed a cavity-type MDR reactor with a hemispherical absorber and secondary concentrator, reaching 30.88% optical-thermal efficiency using a porous Ni/Al<sub>2</sub>O<sub>3</sub> catalyst. Compared to commonly used particle catalysts, porous catalysts exhibit superior catalytic performance and stability.

In this study, a kilowatt-scale solar reactor was designed to receive solar energy for driving the MDR reaction. A new porous Ni/CeO<sub>2</sub> catalyst was synthesized, and the thermochemical characteristics of the reactor under varying flow conditions were investigated, including the conversion rates of CH<sub>4</sub> and CO<sub>2</sub>, as well as the solar-to-fuel conversion efficiency. Study findings provide both the theoretical basis and technical pathway for the efficient and stable utilization of solar energy in large-scale solar–natural gas hybrid fuel production systems.

## 2. EXPERIMENTAL SYSTEM AND PROCEDURE

To investigate the performance of solar-driven MDR for fuel production under concentrated solar irradiation, an efficient Ni/CeO<sub>2</sub> porous catalyst was synthesized for reaction. In addition, a prototype experimental platform was designed and constructed.

### 2.1 Catalyst preparation

Catalyst synthesis and shaping are shown in Fig. 1. Ce(NO<sub>3</sub>)<sub>3</sub>·6H<sub>2</sub>O was first calcined to form CeO<sub>2</sub>. Then, 1.01 g of Ni(NO<sub>3</sub>)<sub>2</sub>·6H<sub>2</sub>O was dissolved in 1.2 mL deionized water and mixed with 1.8 g of CeO<sub>2</sub> powder. The mixture was stirred for 30 min and aged for 12 h, then dried at 110 °C for 12 h. The dried solid was ground and calcined at 500 °C for 3 h to yield NiO/CeO<sub>2</sub>. The catalyst slurry was repeatedly coated onto the template, which was later removed by calcination.

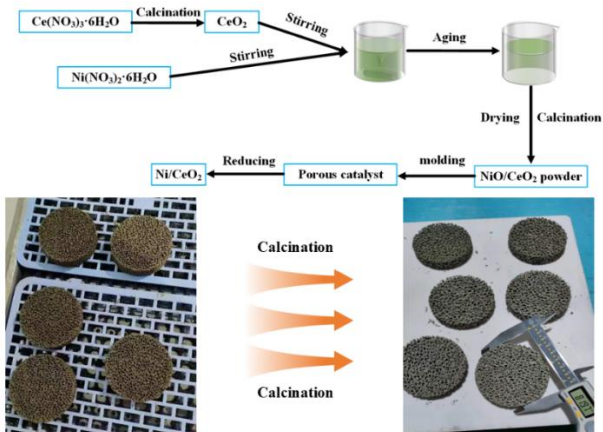


Fig. 1 The preparation and shaping process of the catalyst

### 2.2 Experimental procedures and evaluation indicators

The experimental setup is shown in Fig. 2. A solar simulator provided adjustable light intensity, focused onto the reactor's quartz window using laser alignment. Leak testing was done by sealing the reactor, pressurizing it with N<sub>2</sub> to 0.2 MPa, and confirming no drop over 15 minutes. Before the experiment, the reactor was purged with N<sub>2</sub> at 300 mL/min for 20 min. Once heated to 600 °C, H<sub>2</sub> was introduced for catalyst reduction over 2 h, followed by a 1 h N<sub>2</sub> purge. In this experiment, the CO<sub>2</sub>/CH<sub>4</sub> molar ratio was set to 1.5 for reducing coke formation while maintaining a reasonable CO<sub>2</sub> conversion rate. Product gases were condensed, separated, and analyzed via gas chromatography. The porous catalyst mass was 450 g. CH<sub>4</sub> feeding rate was increased from 1400 to 2200 mL/min, and CO<sub>2</sub> feeding rate was also increased from 2100 to 3300 mL/min. The reactions involved are as follows:

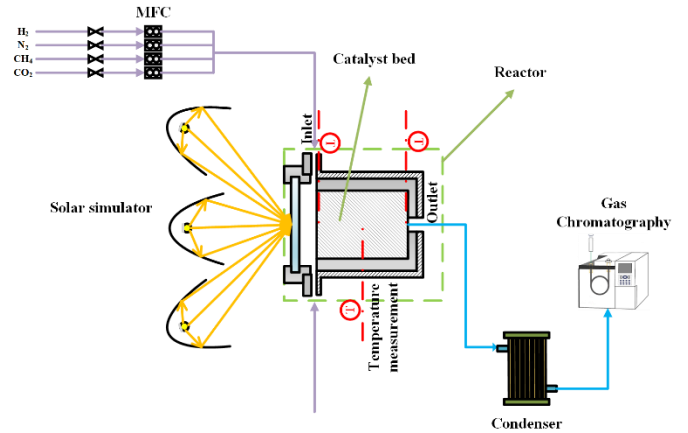
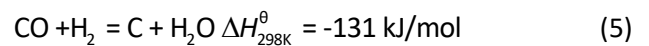
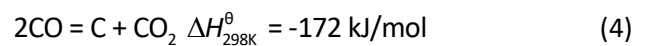
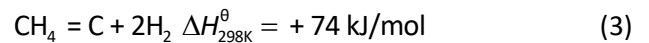
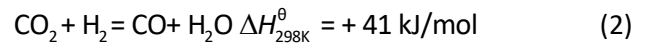
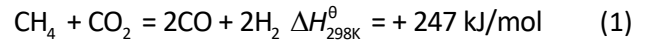


Fig. 2 Experimental system for solar-driven MDR fuel production

The performance evaluation of the concentrated solar-driven MDR reaction includes CH<sub>4</sub> and CO<sub>2</sub> conversion rates, the production rates of H<sub>2</sub> and CO, reaction selectivity, and solar-to-fuel conversion efficiency. The conversion rates of CH<sub>4</sub> and CO<sub>2</sub> can be calculated by:

$$X_{\text{CH}_4} = \frac{F_{\text{CH}_4, \text{in}} - F_{\text{CH}_4, \text{out}}}{F_{\text{CH}_4, \text{in}}} \times 100\% \quad (6)$$

$$X_{\text{CO}_2} = \frac{F_{\text{CO}_2, \text{in}} - F_{\text{CO}_2, \text{out}}}{F_{\text{CO}_2, \text{in}}} \times 100\% \quad (7)$$

$\frac{H_2}{CO}$  is the molar ratio of  $H_2$  to  $CO$ , which is used to

indicate the selectivity for the MDR reaction:

$$\frac{H_2}{CO} = \frac{F_{H_2,out}}{F_{CO,out}} \quad (8)$$

The solar-to-fuel conversion efficiency is calculated by:

$$\eta_{STF} = \frac{F_{H_2,out} \cdot \Delta H_{H_2} + F_{CO,out} \cdot \Delta H_{CO} - F_{CH_4,in} \cdot \Delta H_{CH_4}}{P} \quad (9)$$

where  $F_{CH_4,in}$  (mol/s) and  $F_{CO_2,in}$  (mol/s) are the molar flow rates of  $CH_4$  and  $CO_2$  at the reactor inlet, respectively;  $F_{CH_4,out}$  (mol/s),  $F_{CO_2,out}$  (mol/s),  $F_{H_2,out}$  (mol/s), and  $F_{CO,out}$  (mol/s) are the molar flow rates of the respective outlet gases of  $CH_4$ ,  $CO_2$ ,  $H_2$ , and  $CO$ , respectively.  $\frac{H_2}{CO}$  is the molar ratio of  $H_2$  to  $CO$ ;  $\Delta H_{H_2}$  (286.4 kJ/mol),  $\Delta H_{CO}$  (283 kJ/mol), and  $\Delta H_{CH_4}$  (890.3 kJ/mol) are the standard heats of combustion for  $H_2$ ,  $CO$ , and  $CH_4$ , respectively;  $P$  (kW) is the input power, which is fixed at 1.1 kW and obeys the Gaussian distribution.

### 3. RESULTS AND DISCUSSION

#### 3.1 Energy input and catalyst characterization

The incident light is provided by a solar simulator, which then forms a Gaussian distribution on the incident plane. The distribution results, measured by a Gordon meter, are shown in Fig. 3, with a total input power of 1.1 kW.

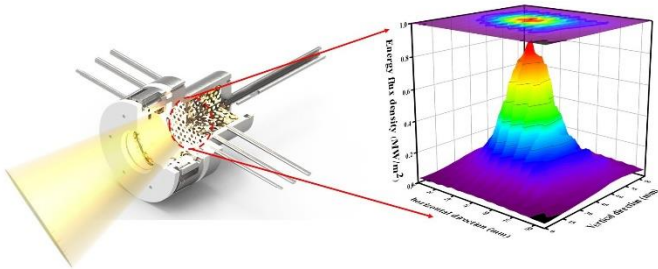


Fig. 3 Energy flux density distribution

The morphology of the porous  $Ni/CeO_2$  catalyst is shown in Fig. 4(a), presenting the open-cell foam structure and pillar network with a pore size of about 2-3 mm. Fig. 4(b) shows the SEM image of the catalyst. From the image, the active components are composed of nm-sized particles, which are supported on the  $CeO_2$  carrier and agglomerate at the micron scale, showing a uniform distribution. Fig. 4(c)-(f) present the elemental mapping results of the catalyst, indicating that O, Ni and Ce are uniformly distributed within the catalyst.

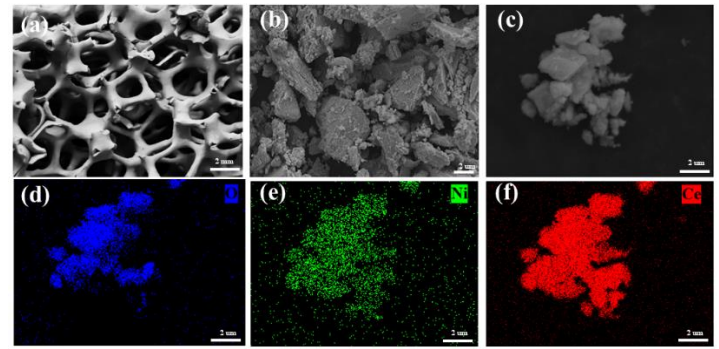


Fig. 4 Morphology of the porous  $Ni/CeO_2$  catalyst (a), SEM image (b), Elemental mapping area (c), EDS mapping image of O (d), EDS mapping image of Ni (e), and EDS mapping image of Ce (f)

#### 3.2 Activity tests

The conversion rates of  $CH_4$  and  $CO_2$  with respect to the  $CH_4$  feeding rate are shown in Fig. 5. It can be observed that the  $CH_4$  conversion rate decreases with the increase of feeding rates, dropping from 78.12% to 65.87%. In contrast, the  $CO_2$  conversion rate fluctuates downward with changes in  $CH_4$  feeding rates. This fluctuation may be due to the occurrence of the side reaction, reverse water-gas shift (RWGS). As the feeding rate increases, the  $H_2$  production rate in the reactor also increases, leading to more interactions with  $CO_2$ . When the  $CH_4$  feeding rate is between 1400 mL/min and 2000 mL/min, the  $CO_2$  conversion rate fluctuates around 65.00%. When the  $CH_4$  feeding rate increases further to 2200 mL/min, the  $CO_2$  conversion rate decreases to 60.15%. This implies that the feeding rate has a greater impact on  $CO_2$  conversion than the side reaction.

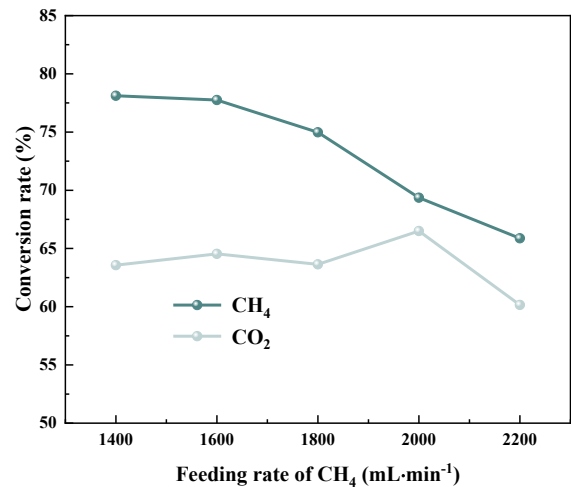


Fig. 5 The conversion rates of  $CH_4$  and  $CO_2$  in the porous catalyst with the  $CH_4$  feeding rate

The production rates of  $H_2$  and  $CO$ , as well as the  $H_2/CO$  ratio under different feeding conditions, are shown in Fig. 6. When the  $CH_4$  feeding rate increases from 1400 mL/min to 2200 mL/min, the  $H_2$  production

rate increases from 2.14 L/min to 2.68 L/min, and the CO production rate increases from 2.63 L/min to 3.53 L/min. Moreover, the H<sub>2</sub>/CO ratio decreases with the increase in CH<sub>4</sub> feeding rate. The increase in feeding rate likely changes the gas distribution within the reactor, leading to higher concentrations of CO<sub>2</sub> and H<sub>2</sub>, thereby promoting the RWGS reaction rate. Additionally, the increase in feeding rate causes temperature changes within the reactor, which is one of the important factors affecting the H<sub>2</sub>/CO ratio. Reactions occurring on the surface of the porous catalyst exhibit higher selectivity towards CO generation.

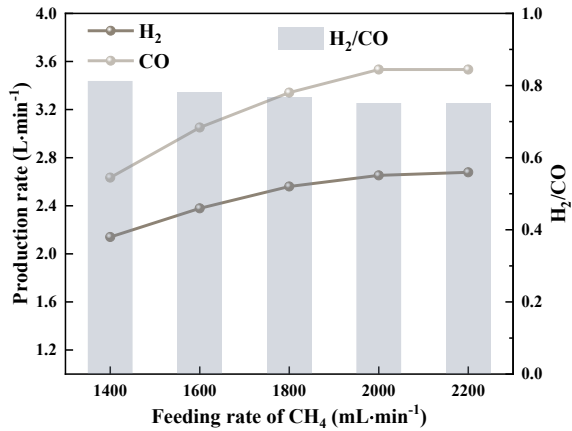


Fig. 6 Production rates of H<sub>2</sub> and CO and their molar ratio

Fig. 7 shows the variation of reactor average temperature and solar-to-fuel conversion efficiency with CH<sub>4</sub> feeding rate. At a CH<sub>4</sub> feeding rate of 1400 mL/min, the reactor's average temperature is 780 °C, decreasing to 725 °C as the rate increases to 2200 mL/min. With the porous catalyst, higher feeding rates cause greater temperature drops, reducing MDR reaction selectivity and thereby impacting overall efficiency. At a CH<sub>4</sub> feeding rate of 1400 mL/min, the efficiency is lowest at 26.10%. As the feeding rate increases, the efficiency first rises, reaching a peak of 33.26% at 2000 mL/min, then decreases slightly to 32.36% at 2200 mL/min. This occurs because, while higher feeding rates reduce reactor temperature, the rapid initial increase in H<sub>2</sub> and CO yields enhances solar-to-fuel conversion efficiency. Beyond a certain point, the increase in H<sub>2</sub> and CO production slows down, while more heat is carried out by the gas mixture, increasing thermal losses and reducing overall efficiency.

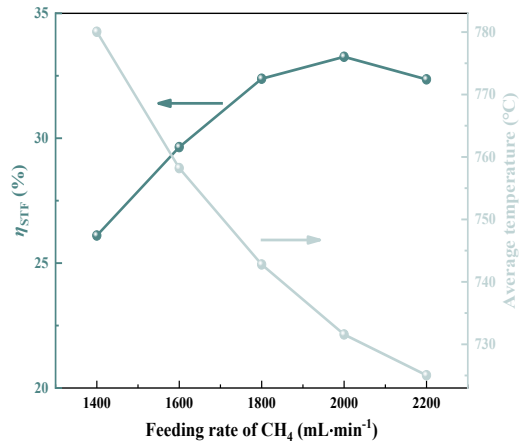


Fig. 7  $\eta_{STF}$  and reactor average temperature as a function of CH<sub>4</sub> feeding rate

A stability test was performed on the porous catalyst under the condition of a CH<sub>4</sub> feeding rate of 2000 mL/min. In Fig. 7, the solar-to-fuel conversion efficiency reached a peak at this point. From Fig. 8, it can be seen that during the stability test, the conversion rates of CH<sub>4</sub> and CO<sub>2</sub> exhibited slight fluctuation, and the system achieved stable operation for up to 8 hours. Under these conditions, the catalyst did not show significant deactivation, validating its advantage for long-term stable operation.

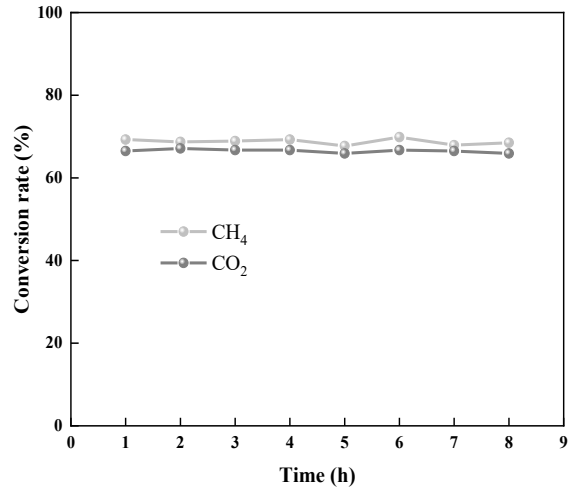


Fig. 8 Stability operation test

### 3.3 Great potential of porous Ni/CeO<sub>2</sub> in solar-driven MDR reactions

From the perspective of maximizing solar energy utilization,  $\eta_{STF}$  reached its highest value of 33.26% when the CH<sub>4</sub> feeding rate was 2000 mL/min and the CO<sub>2</sub> feeding rate was 3000 mL/min. The methane conversion rate was 69.36%, and the CO<sub>2</sub> conversion rate was 66.50%. The  $\eta_{STF}$  was compared with some internationally leading studies, as shown in Table. 1. It can be seen that the experimental scales of these studies are generally small, with methane feeding rates not

exceeding 50 mL/min. In contrast, the solar-driven MDR experimental platform developed in this study not only scaled up the experiment, increasing the methane feeding rate to the L/min level, but also achieved a higher solar-to-fuel conversion efficiency. This highlights the remarkable potential of the porous Ni/CeO<sub>2</sub> catalyst in solar-driven MDR reactions, offering valuable insights into industrial applications of solar-thermal coupled MDR in fuel production.

*Table. 1  $\eta_{STF}$  benchmarks in solar-driven MDR*

Catalyst	CH <sub>4</sub> feeding rate (mL/min)	$\eta_{STF}$ (%)	Reference
Ni-CeO <sub>2</sub> /SiO <sub>2</sub>	5.05	27.4	[14]
Co/Co-Al <sub>2</sub> O <sub>3</sub>	26.76	27.1	[15]
Ni/Mg-Al <sub>2</sub> O <sub>3</sub>	26.34	32.5	[16]
NiCo alloy	44.42	33.8	[17]
Ni-psnts@CeO <sub>2</sub>	30.32	36.9	[18]
Ni/CeO <sub>2</sub>	2000	33.26	This study

#### 4. CONCLUSIONS

This study developed a kilowatt-scale solar-driven MDR system to maximize the utilization of solar energy for fuel production. The research synthesizes new porous Ni/CeO<sub>2</sub> catalysts for enhancing the thermochemical performance of the MDR reaction under varying feeding rates of CH<sub>4</sub> and CO<sub>2</sub>. The results demonstrated that the highest  $\eta_{STF}$  of 33.26% is achieved. The system operated continuously for over 8 hours without significant catalyst deactivation, showing the catalyst's robustness and long-term performance in solar-driven processes. These findings present novel approaches for the effective and stable use of solar energy in large-scale MDR reactions, providing valuable guidance for industrial applications of solar-driven methane reforming for fuel production.

#### ACKNOWLEDGEMENT

The authors are grateful for the support provided by the National Key Research and Development Program of China (2021YFF0500701), the Major Program of the National Science Foundation of China (No. 52090061), and the National Science Fund for Distinguished Young Scholars (No. 52225601).

#### REFERENCE

[1] Zhang Y, Li Q, Qiu Y. Optical-thermal-stress analysis of a multiscale solar receiver for ultra-high-temperature concentrating solar power. *Journal of Cleaner Production* 2023;433:139791. <https://doi.org/10.1016/j.jclepro.2023.139791>.

[2] Li J, Chen X, Li G. Effect of separation wavelength on a novel solar-driven hybrid hydrogen production system (SDHPS) by solar full spectrum energy. *Renewable Energy* 2023;215:118969. <https://doi.org/10.1016/j.renene.2023.118969>.

[3] Lu B, Liu T, Yan X, Zheng Z, Liu Q. A new solar mid-and-low temperature receiver/reactor with linear Fresnel reflector. *Applied Thermal Engineering* 2023;226:120216. <https://doi.org/10.1016/j.applthermaleng.2023.120216>.

[4] Ma Z, Li M-J, He Y-L, Zhang KM. Effects of partly-filled encapsulated phase change material on the performance enhancement of solar thermochemical reactor. *Journal of Cleaner Production* 2021;279:123169. <https://doi.org/10.1016/j.jclepro.2020.123169>.

[5] Yadav D, Banerjee R. A review of solar thermochemical processes. *Renewable and Sustainable Energy Reviews* 2016;54:497–532. <https://doi.org/10.1016/j.rser.2015.10.026>.

[6] Noor ZZ, Yusuf RO, Abba AH, Abu Hassan MA, Mohd Din MF. An overview for energy recovery from municipal solid wastes (MSW) in Malaysia scenario. *Renewable and Sustainable Energy Reviews* 2013;20:378–84. <https://doi.org/10.1016/j.rser.2012.11.050>.

[7] Gao Y, Jiang J, Meng Y, Yan F, Aihemaiti A. A review of recent developments in hydrogen production via biogas dry reforming. *Energy Conversion and Management* 2018;171:133–55. <https://doi.org/10.1016/j.enconman.2018.05.083>.

[8] Liu C, Bian J, Zhang G, Li D, Liu X. Influence of optical parameters on thermal and optical performance of multi-layer glazed roof filled with PCM. *Applied Thermal Engineering* 2018;134:615–25. <https://doi.org/10.1016/j.applthermaleng.2018.01.117>.

[9] Shi X, Shuai Y, Wang F, Zhang C, Cheng Z, Chen X. Effects of ordered hierarchically porous structure on methane reforming performance in solar foam reactor. *Journal of CO<sub>2</sub> Utilization* 2020;37:147–57. <https://doi.org/10.1016/j.jcou.2019.12.002>.

[10] Yang H, Yan S, Yao D, Luo H, Zeng K, Li J, et al. Photo-thermal catalytic pyrolysis of waste plastics: Investigation into light-induced metal-support interaction. *Fuel* 2023;333:126496. <https://doi.org/10.1016/j.fuel.2022.126496>.

[11] Shi X, Zhang X, Wang F, Yang L, Dong Y, Shuai Y. Thermochemical analysis of dry methane reforming hydrogen production in biomimetic venous hierarchical porous structure solar reactor for improving energy storage. *International Journal of Hydrogen Energy* 2021;46:7733–44. <https://doi.org/10.1016/j.ijhydene.2020.12.034>.

- [12] Zhang H, Shuai Y, Lougou BG, Jiang B, Wang F, Cheng Z, et al. Effects of multilayer porous ceramics on thermochemical energy conversion and storage efficiency in solar dry reforming of methane reactor. *Applied Energy* 2020;265:114799. <https://doi.org/10.1016/j.apenergy.2020.114799>.
- [13] Zhang W, Li Q, Qiu Y. Design and optimization of a solar-driven methane dry reforming reactor by developing an optical-thermal-chemical model. *Chemical Engineering Journal* 2024;483:149094. <https://doi.org/10.1016/j.cej.2024.149094>.
- [14] Jiang Z, Li Y, Zhang Q, Yang Y, Wu S, Wu J, et al. A novel nanocomposite of mesoporous silica supported ni nanocrystals modified by ceria clusters with extremely high light-to-fuel efficiency for UV-vis-IR light-driven CO<sub>2</sub> reduction. *J Mater Chem A* 2019;7:4881–92. <https://doi.org/10.1039/C9TA00259F>.
- [15] Wu S, Li Y, Zhang Q, Jiang Z, Yang Y, Wu J, et al. High light-to-fuel efficiency and CO<sub>2</sub> reduction rates achieved on a unique nanocomposite of co/co doped Al<sub>2</sub>O<sub>3</sub> nanosheets with UV-vis-IR irradiation. *Energy Environ Sci* 2019;12:2581–90. <https://doi.org/10.1039/C9EE01484E>.
- [16] Tan X, Wu S, Li Y, Zhang Q, Hu Q, Wu J, et al. Highly efficient photothermocatalytic CO<sub>2</sub> reduction in ni/mg-doped Al<sub>2</sub>O<sub>3</sub> with high fuel production rate, large light-to-fuel efficiency, and good durability. *Energy & Environ Materials* 2022;5:582–91. <https://doi.org/10.1002/eem2.12193>.
- [17] Liu X, Shi H, Meng X, Sun C, Zhang K, Gao L, et al. Solar-enhanced CO<sub>2</sub> conversion with CH<sub>4</sub> over synergistic NiCo alloy catalysts with light-to-fuel efficiency of 33.8%. *Solar RRL* 2021;5:2100185. <https://doi.org/10.1002/solr.202100185>.
- [18] Shi H, Tian C, Liu X, Sun N, Song C, Zheng H, et al. Ni-phyllsilicate nanotubes coated by CeO<sub>2</sub> for ultra-efficiency of 36.9% and near-limit CO<sub>2</sub> conversion in solar-driven conversion of CO<sub>2</sub>-to-fuel. *Chemical Engineering Journal* 2023;454:140063. <https://doi.org/10.1016/j.cej.2022.140063>.